

High pressure structural and magneto-transport studies on type-II Dirac semimetal candidate $\text{Ir}_2\text{In}_8\text{S}$: Emergence of superconductivity upon decompression

Pallavi Malavi,^{1,*} Prakash Kumar,² Navita Jakhar,² Surjeet Singh,² and S. Karmakar¹

¹*High Pressure and Synchrotron Radiation Physics Division,
Bhabha Atomic Research Centre, Trombay, Mumbai 400085, India*

²*Department of Physics, Indian Institute of Science Education and Research (IISER), Pune 411008, India
(Dated: May 23, 2022)*

The structural and magneto-transport properties of type-II Dirac semimetal candidate $\text{Ir}_2\text{In}_8\text{S}$ have been investigated under high pressure. The ambient tetragonal structure ($P4_2/mnm$) is found to be stable up to ~ 7 GPa, above which the system takes an orthorhombic $Pnmm$ structure, possibly destroying the Dirac cones due to the loss of the four-fold screw symmetry. In the tetragonal structure, a gradual suppression of the transverse magneto-resistance and a rapid change in the magnetic field dependence above 50K suggest possible T -dependent Fermi surface modification. In the high pressure phase, the metallic character increases marginally (as evident from the increased RRR value) accompanied with suppressed magneto-resistance, without emergence of superconductivity up to 20 GPa and down to 1.4K. Most surprisingly, upon release of pressure to 0.2 GPa, a sharp resistance drop below ~ 4 K is observed, field varying measurements confirm this as the onset of superconductivity. The observed changes of the carrier density and mobility in the pressure-released tetragonal phase indicate electronic structural modification resulting from the irreversible polyhedral distortion. A simultaneous increase in the residual resistivity and carrier density upon decompression indicates that an enhanced impurity scattering play a key role in the emergence of superconductivity in the tetragonal $\text{Ir}_2\text{In}_8\text{S}$, making it an ideal platform to study topological superconductivity.

PACS numbers:

I. INTRODUCTION

Three dimensional Dirac semimetals (DSM) are new states of topological quantum matter, characterized by symmetry-protected linear band crossing at the 4-fold degenerate Dirac point near the Fermi level.^{1,2} The massless Dirac fermions arising from Dirac points are often considered responsible for the remarkable transport properties, including ultrahigh carrier mobility as a result of topology-protected suppression of backscattering and extremely large and unusual field and angle dependent magneto-resistance (MR) in 3D materials like Cd_3As_2 ,^{3,4} Na_3Bi ,^{5,6} TlBiSeS ⁷ and PtBi_2 .⁸ Weyl semimetals (WSM) are topological semimetals where either inversion symmetry or the time reversal symmetry breaking causes splitting of the Dirac point into chiral Weyl nodes having different surface states and Fermi arcs than DSM.⁹ Nonmagnetic WSMs in the TaAs-family, hosting Weyl fermions and featuring chiral magnetic anomaly, also exhibit ultrahigh mobility and extreme magnetoresistance (XMR).^{10–13} The XMR has been reported in the Lorentz invariance-broken (type-II) WSM candidates WTe_2 , WP_2 , MoTe_2 ^{14–18} and in Dirac line-node semimetals.^{19–22} Understanding the remarkable transport properties in terms of non-trivial band topology is often debated. While electron-hole compensation mechanism is considered a necessary ingredient for the emergence of the XMR in multiband semimetals,^{14,23–26} the possible origin of the ultrahigh mobility (the most essential criteria) is discussed in terms of either topological protection^{4,5,11,27,28} or spin-orbit coupling (SOC)-

induced orbital texture on Fermi surface.^{16,25,29–31}

Lorentz invariance-broken (type-II) DSM state, as has been predicted and experimentally verified in the $1T$ - PtSe_2 -family^{32,33} and VAL_3 -family,³⁴ has become of tremendous current research interest due to the observed finite density of states around the Dirac point, that may help emerge topological superconductivity in the surface states and host Majorana modes with possible applications in quantum computations.³⁵ The non-trivial topology has indeed been established in the superconducting (SC) phases of PdTe_2 and $\text{Ir}_{1-x}\text{Pt}_x\text{Te}_2$.^{36–38} However, the normal state MR and so the carrier mobility are found much reduced in these compounds, implying non-involvement of the massless Dirac fermions in the transport phenomena. It is noteworthy that the observed SC in the type-I DSM Cd_3As_2 at high pressure is accompanied by a structural transition³⁹ and SC emerges in WTe_2 at high pressure with complete suppression of MR,^{40,41} suggesting possible non-coexistence of the SC state and the topological surface states. Tremendous efforts are thus being continued in search of new and diverse type-II DSM with remarkable transport properties, as possible platform to explore topological superconductivity.

Subchalcogenide compounds with diverse structural motifs have recently been found to be promising topological semimetal candidates.^{2,42–44} The sub-valent metallic character in related compounds also leads to competing electronic phases like charge density wave (CDW) and superconductivity.^{45,46} Recently, type-II Dirac semimetal candidate subchalcogenides $\text{Ir}_2\text{In}_8\text{Q}$ ($\text{Q}=\text{S}, \text{Se}, \text{Te}$) have been grown successfully and are also found to exhibit sig-

nificantly large and anisotropic MR (qualifying the ultra-high mobility criteria).^{43,44} $\text{Ir}_2\text{In}_8\text{S}$ compounds crystallize in tetragonal $P4_2/mnm$ space group with 3D framework of IrIn_8 polyhedra with chalcogen atoms in the channels along the c -axis. No superconductivity has been reported in this series of compounds. But an increased chalcogen atom radii leads to lattice instability with commensurately modulated structures due to enhanced polyhedral distortions at intermediate temperatures. This also reduces the low temperature magnetoresistance.⁴⁴ As the effect of pressure is expected to be similar to that of decreasing atomic radii, high pressure study on these compounds may reveal competing electronic phases, including superconductivity. Also the band structure calculations show that the two sets of Dirac points in $\text{Ir}_2\text{In}_8\text{S}$ are situated ~ 25 and ~ 40 meV above the Fermi level.⁴³ Pressure-induced band broadening may shift the Fermi level upward by enhancing the carrier density and help tune the Fermi level towards the Dirac points, thus possibly exhibiting exotic transport signatures.

We report here the effect of pressure on the structural and magneto-transport properties of subsulfide $\text{Ir}_2\text{In}_8\text{S}$. The ambient tetragonal structure ($P4_2/mnm$) is stable up to ~ 7 GPa, above which the system takes an orthorhombic $Pnmm$ structure. A loss of the four-fold screw symmetry in the high P structure possibly destroys the Dirac cones making it a trivial semimetal. In the tetragonal structure, a drastically suppressed MR at high T and the change in its field dependence suggests significant Fermi surface (FS) modification with increasing temperature. The characteristic temperature T^* , below which local polyhedral distortion ceases, decreases upon increasing P . In the high P orthorhombic phase, the metallicity increases marginally and the magneto-resistance gets suppressed. No superconductivity has been observed down to 1.4K up to ~ 20 GPa. Surprisingly, upon decompression to 0.2 GPa a sharp resistance drop is noticed below ~ 4 K, indicating superconductivity onset in the pressure-released sample. The magneto-transport properties show significant change of the carrier density and mobility, suggesting electronic structural modification due to subtle polyhedral rearrangement upon P -cycling. An enhanced impurity scattering may have an important role in the emergence of SC in the ambient tetragonal structure (that supports type-II Dirac semimetal state), making tetragonal $\text{Ir}_2\text{In}_8\text{S}$ an ideal platform to study topological superconductivity at ambient pressure.

II. EXPERIMENTAL METHODS

High quality single crystal $\text{Ir}_2\text{In}_8\text{S}$ has been synthesized using indium metal flux method⁴⁴ and characterized by x-ray diffraction, EDX and HRTEM measurements (discussed in Supplementary Material).⁴⁷ High-pressure powder x-ray diffraction measurements at room temperature have been performed at the XPRESS beam

line ($\lambda = 0.4957\text{\AA}$) of the Elettra synchrotron, Trieste. Single crystals were finely powdered and loaded in a diamond anvil cell (DAC) for measurements under quasi-hydrostatic pressures with methanol-ethanol-water (MEW) (16:3:1) as pressure transmitting medium (PTM) and Cu as x-ray pressure marker.⁴⁸ The 2D diffraction images were recorded on a Mar345 image plate detector and these were converted to $I - 2\theta$ diffraction profiles using the Fit2D software.⁴⁹ Structural analyses were performed using EXPGUI software.⁵⁰

High-pressure resistance measurements at low temperatures have been performed on a freshly cleaved ~ 20 μm thick microcrystal of ~ 100 μm lateral dimension (cleaved plane have arbitrary crystallographic orientation). A Stuttgart version DAC was used for measurements under quasi-hydrostatic pressures up to 20 GPa using NaCl as the PTM. The resistance was measured using standard four probe method with 1 mA current excitation and in the ac lock-in detection technique. For measurements down to 1.4 K, the DAC was placed inside a KONTI-IT (Cryovac) cryostat. A nonmagnetic Cu-Be DAC (M/s EasyLab) was prepared with identical sample size for high-field measurements under quasi-hydrostatic pressures up to 7.5 GPa and was inserted into a S700X SQUID magnetometer (M/s Cryogenic Ltd) to study transverse MR and Hall resistance up to 7T field. Pressures were measured by conventional ruby luminescence method.

III. RESULTS AND DISCUSSION

Powdered diffraction patterns at various high pressures are shown in Figure 1a. The ambient tetragonal structure (SG: $P4_2/mnm$) of $\text{Ir}_2\text{In}_8\text{S}$ is found to be stable up to ~ 7 GPa. Structural analyses at various high pressures have been performed by Le-Bail profile fitting,⁴⁷ using the reported atomic coordinates.⁴⁴ For pressures above 7GPa, the system undergoes a subtle structural transition to a low symmetric orthorhombic structure ($Pnmm$), as determined by the group-subgroup analysis. In Figure 1(b,c) are shown the variation of lattice parameters and the unit cell volume as a function of pressure, showing $\sim 2\%$ volume collapse across the structural transition (indicating first order nature of the phase transition). $P - V$ data when fitted with the 3rd order Birch-Murnaghan equation of state gives bulk moduli 85(4) GPa ($B'=4.1$) and 104(5) GPa ($B'=5$) in the tetragonal and orthorhombic phases respectively. Due to our inability to refine all the In atom positions in the structural analysis of the XRD patterns at high pressures, we cannot comment on the pressure evolution of the IrIn_8 polyhedral distortions. Upon release of pressure, the orthorhombic phase transforms back completely to the ambient tetragonal structure, also regaining the initial Bragg peak width (indicating absence of any apparent structural disorder).⁴⁷

High pressure resistance data up to ~ 20 GPa measured on the single crystal $\text{Ir}_2\text{In}_8\text{S}$ (along an arbitrary crystal-

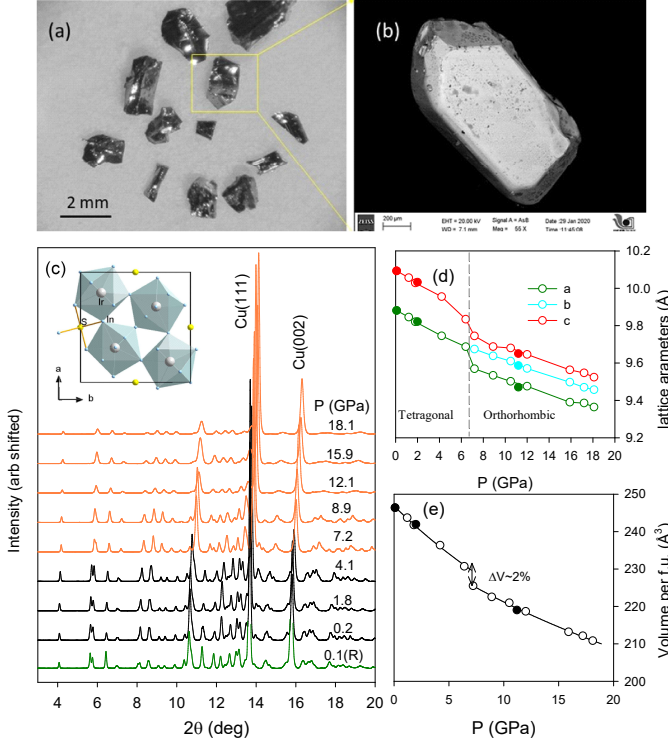


FIG. 1: (Color online) (a) A few representative single crystal specimens of Ir₂In₈S. (b) FESEM image of one of the specimens. (c) Powder x-ray diffraction patterns at various high pressures. Patterns in red correspond to the orthorhombic structures above 7 GPa. Released pattern at 0.1 GPa is shown in green. Inset shows the polyhedral arrangement in the tetragonal unit cell. Variation of lattice parameters (d) and volume per formula unit (e) are plotted as a function of *P*, solid circles are for releasing pressures.

lographic plane) in the temperature range 1.4-300K are shown in Figure 2(a,c). No superconductivity has been observed down to 1.4 K. At 0.2 GPa, $R(T)$ displays an overall metallic behavior, with anomalous kink feature at the characteristic temperature ($T^* \sim 230$ K), above which local disordering in the IrIn₈ polyhedra emerges, agreeing well with the previous reported data.⁴⁴ The presence of noticeable hysteresis at high *T* (shown as inset in Figure 2a) supports the structural origin of this resistance anomaly. In the ordered phase (below T^*) the resistance $R(T)$ above 30K follows the Bloch-Grüneisen (BG) resistivity model⁵¹

$$\rho(T) = \rho_0 + C \left(\frac{T}{\Theta_D} \right)^k \int_0^{\Theta_D/T} \frac{x^k}{(e^x - 1)(1 - e^{-x})} dx$$

where ρ_0 is the residual resistivity and Θ_D is the Debye temperature. The $R(T)$ data for pressures up to 5 GPa can be fit well with $k=5$, indicating phonon dominated scattering mechanism. At 0.2 GPa, $\Theta_D=214$ K, in reasonable agreement with the reported value.⁴⁴ The $R(T)$ data above 30K at 8 GPa (in the orthorhombic phase) when fitted with the BG equation gives $k=4.1$

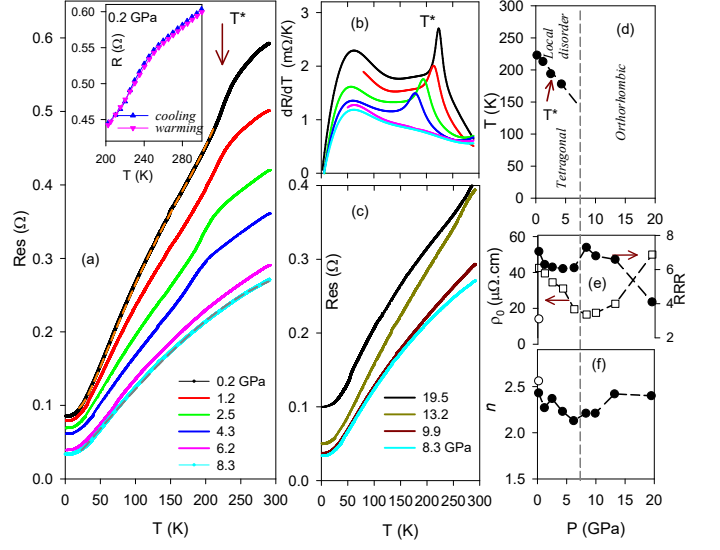


FIG. 2: (Color online) (a) $R(T)$ plots at various high pressures up to 8.3 GPa. Dashed lines are the BG fit for the $R(T)$ data at 0.2 GPa and 8.3 GPa. Inset, $R(T)$ behavior near the onset of local disorder in cooling and warming cycle. (b) dR/dT plots showing systematic decrease of T^* . (c) $R(T)$ plots at higher pressures up to 19.5 GPa (d) *P* – *T* structural phase diagram of Ir₂In₈S. (e,f) Pressure variation of the residual resistivity, the RRR value and the exponent *n* in the power-law fit of $R(T)$ below 20K.

with $\Theta_D=120$ K, indicating significant electronic structural modifications.

In Figure 2b are shown the dR/dT plots at various pressures. The characteristic temperature (T^*) down to which the random polyhedral disorder persists in the tetragonal structure, as indicated by the peak position, systematically decreases due to enhanced intrinsic disorder in the system at higher pressures. In the high pressure orthorhombic phase, the resistance anomaly disappears indicating ordered polyhedral arrangements. Figure 2d summarizes the structural phase diagram of Ir₂In₈S, based on the XRD and resistance measurements. At a low pressure (0.2 GPa), $R(T)$ data below 20K, fitted with power law $\rho(T) = \rho_0 + A_1 T^n$ gives $n \sim 2.5$ indicating electron-electron dominated scattering along with inter-band electron-phonon scattering.⁵¹ Although the residual resistivity ρ_0 in the tetragonal structure decreases significantly with pressure, the residual resistivity ratio (RRR) and so the metallic character remains mostly unchanged up to 5 GPa. An order of magnitude less RRR value in our DAC-based measurement, compared to the reported value on the bare sample⁴³ (that were measured in the ab-plane), can be attributed to the arbitrary crystallographic orientation of the measurement plane. The metallicity (as seen from the RRR values) marginally increases across the transition to the orthorhombic phase but decreases more rapidly at higher pressures (Figure 2e). In the tetragonal phase, *n* decreases systematically with increasing *P* and approaches the Fermi Liquid be-

havior ($n = 2$) near the structural transition, with opposite trend noticed in the orthorhombic phase [Figure 2f]. The structural transition is thus associated with a significant change in the electronic structure. Moreover, in the high pressure orthorhombic structure ($Pn\bar{m}$), the four-fold screw 4_2 symmetry (that protects Dirac point linear band crossing in the tetragonal structure)⁴⁴ is lost, suggesting a possible quantum topological transition associated with the structural transition.

First, we show the temperature dependence of resistivity in $\text{Ir}_2\text{In}_8\text{S}$ at a low pressure (0.5 GPa) in different magnetic fields applied perpendicular to the current plane (see Figure 3a). With the application of the magnetic field, $\rho(T)$ shows a large upturn which saturates below ~ 20 K. The $\rho(T)$ is also found to obey the power law T -dependence below ~ 20 K (Figure 3b). The signature is similar to that of known extreme magneto-resistance materials.^{8,11–18,22,31,52,53} Based on the field dependence of $d\rho/dT$ (Figure 3c) we plot the temperature-field phase diagram as inset in Figure 3a, where T_m and T_i are taken as the sign change point and the minimum in $d\rho/dT$.⁵⁴ The phase diagram is also consistent with known XMR materials.³¹ We can note that the order-disorder transition temperature T^* is independent of the applied magnetic field up to 7T, further supporting its structural origin.

Figure 4a,b show the plots of the field dependence of the transverse magneto-resistance $\text{MR}=[R(H)-R(0)]/R(0)$ and the Hall resistance at various temperatures at 0.5 GPa. As the measurements on the flake sample were performed in the van der Pauw method, the observed asymmetry of the MR curves originates from the in-plane Hall contribution that is separated by symmetrizing the MR curves, $\text{MR}_{\text{sym}}(H)=[\text{MR}(H)+\text{MR}(-H)]/2$. An order of magnitude reduced transverse MR in our measurement, compared to the reported value for the ambient sample,⁴³ can be due to the arbitrary crystallographic plane of this high P measurements. Moreover, a small pressure can lead to drastic reduction of MR in XMR materials due to Fermi surface modification.⁵⁵ With increasing temperature, MR decreases rapidly. A highly non-linear field dependent Hall resistance indicates multicarrier transport behavior in $\text{Ir}_2\text{In}_8\text{S}$ (Figure 4b). At low temperature large negative R_{xy} indicates electron dominated transport. At high temperature above 50K, R_{xy} becomes positive overall, showing hole dominating transport. This is also apparent in the T -dependent Hall resistivity measured at 5T field (see inset of Figure 4b, obtained by field reversal and current reversal measurements). The presence of multiple Fermi surfaces in the tetragonal $\text{Ir}_2\text{In}_8\text{S}$ have been reported by quantum oscillation measurements and band structure calculations.⁴³

Field-induced resistivity upturn in the XMR materials can be explained by semiclassical multi-carrier model in systems obeying modified Kohler's rule $\text{MR} = F[H/\rho_0] = A[H/\rho_0]^m$.^{23,25} In case of perfect electron-hole resonance condition, $m=2$.¹⁴ For systems where Kohler's rule⁵⁶ is nearly obeyed ($m \approx 2$ and T -independ-

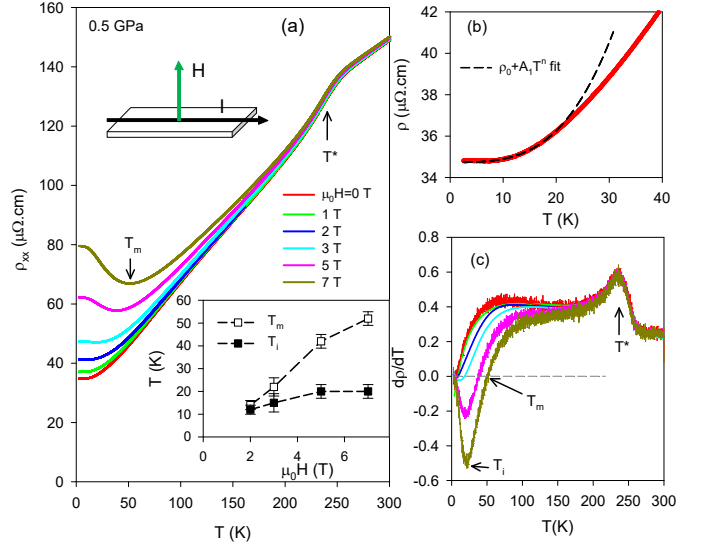


FIG. 3: (Color online) (a) Resistivity ρ_{xx} plotted as a function of temperature at 0.5 GPa under different magnetic fields. Inset, The $T-H$ phase diagram, field variation of the two characteristic temperatures T_i and T_m , as obtained from (c). (b) Zero field $\rho(T)$, obeying the power law fit below 20K. (c) $d\rho/dT$ plots at various fields.

dent), MR is found to scale with A .¹⁶ As shown in Figure 4c, MR in $\text{Ir}_2\text{In}_8\text{S}$ systematically deviates from Kohler's rule above 10K (both A and m varying rapidly with T). At 2.5K, $m=1.58$ (see inset in Figure 4f), similar to other type-II topological semimetals^{16,57}; deviation from the quadratic field dependence ($m < 2$) can be due to un-compensated carriers or anisotropic Fermi surface or field-induced Fermi surface modification.^{15,58} In case of anisotropic multiband materials, relative contribution of different FS pockets also vary with strength and orientation of the magnetic field.^{59,60} Variation of A with temperature, when compared with field-induced resistivity change (shown in Figure 4e), indicates a rapid change of carrier transport behavior below 50K. This is further verified by the observed variation of the exponent m as a function of temperature (Figure 4f) indicating electronic structural modification at low T . The field dependent MR thus follows $\text{MR} \propto (\mu_a H)^m$, where μ_a is the average carrier mobility.

The Hall conductivity σ_{xy} has been obtained using the formula $\sigma_{xy} = [\rho_{xy}/(\rho_{xx}^2 + \rho_{yy}^2)]$, because of the observed isotropic in-plane linear resistivity (ρ_{xx}) and Hall resistivity ρ_{xy} . The carrier density and mobility have been calculated by analyzing the Hall conductivity using two band model⁶¹

$$\sigma_{xy} = eB \left(\frac{n_h \mu_h^2}{1 + \mu_h^2 B^2} - \frac{n_e \mu_e^2}{1 + \mu_e^2 B^2} \right)$$

where n_e (n_h) and μ_e (μ_h) are electron (hole) density and mobility respectively. Figure 4d shows the plots of Hall conductance σ_{xy} at various temperatures. As shown in

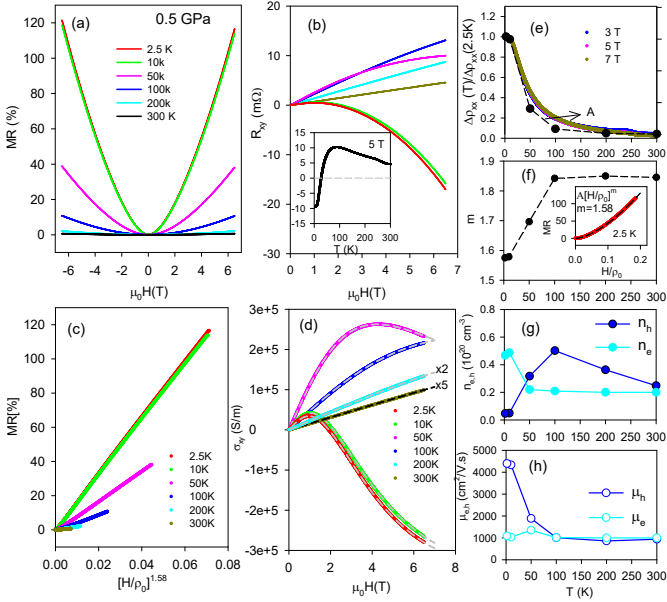


FIG. 4: (Color online) Transverse MR (a) and Hall resistance (b) at 0.5 GPa as a function of applied magnetic field at various temperatures. Inset in (b), temperature dependent Hall resistance at 5 T field. (c) MR vs $[H/\rho_0]^{1.58}$ plots at different T . Above 10 K, curves do not superpose, showing violation of Kohler's rule. (d) Plots of Hall conductivity σ_{xy} . (e) Field-induced normalized resistivity change plotted as a function of T . The A coefficient is found to scale with the resistivity change (f) T -variation of the exponent m . (g,h) T -variation of the carrier density $n_{e,h}$ and mobility $\mu_{e,h}$, as obtained from the Hall conductivity from the two-band model fit.

Figure 4(g,h), at low T the electron density is an order of magnitude higher than the hole density and therefore dominates the transport. But the hole mobility is 4 times higher than the electron mobility at this T . Our results are different than the reported results from the measurements on ab-plane in a bare sample.⁴³ The discrepancy may be attributed to the fact that the sample is under pressure in the present case or intrinsic to the sample quality. The large carrier mobility mismatch and a rapid decrease of hole mobility with increasing T are responsible for the systematic violation of the Kohler's rule with T .

Magneto-resistance (MR) and Hall measurements have been performed up to 7 T field and at pressures up to 7.5 GPa. Figures 5(a-c) show the $\rho(T)$ plots for $B=0$ T and 7 T at 0.5 GPa, 7.5 GPa and at 0.2 GPa (upon decompression). With increasing pressure, the field-induced resistance upturn decreases with dramatic suppression of MR. Upon decompression at 0.2 GPa, the residual resistivity at zero field increases and MR is partially recovered (Figure 5c). To our surprise, we observe a sharp resistance drop below ~ 4 K, that becomes prominent at low current excitation, as can be seen in inset in Figure 5c. This indicates possible onset of superconductivity in the pressure-released sample. It is worth men-

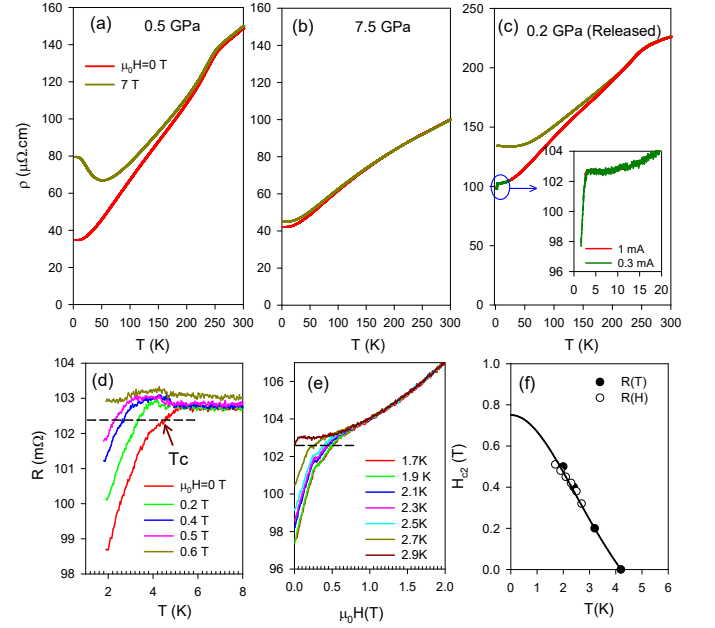


FIG. 5: (Color online) Resistivity $\rho(T)$ at zero field and at 7 T field plotted at (a) 0.5 GPa, (b) 7.5 GPa and (c) at 0.2 GPa (upon decompression). Resistivity drop below ~ 4 K in (c) is shown by blue circle, enlarged view shown as inset. (d) $R-T$ data near SC onset T_c at 0.2 GPa (upon decompression) under different fields up to 0.6 T. (e) $R-H$ data at various T below SC T_c (f) the $H_{c2}-T_c$ plots and the Ginzburg-Landau fit.

tioning that any In precipitation upon P -cycling causing the observed SC is unlikely, as no additional Bragg peaks corresponding to elemental In have been detected in XRD upon P -release.⁴⁷ Also the observed broad transition width and much higher critical field (as shown below) is in contrast to that of bulk In superconductivity. The observed broad SC onset in P -released sample after repeated P -cycling further verifies that SC occurs in the tetragonal $\text{Ir}_2\text{In}_8\text{S}$ and rules out the possibility of sample decomposition.⁴⁷ Noting that $\text{Ir}_2\text{In}_8\text{S}$ is prone to disorder due to IrIn_8 polyhedral distortion, the observed enhanced residual resistivity in the normal state may be attributed to the increased defect/impurity scattering or the electronic structural modification due to subtle structural rearrangements that has not been detected by XRD. The impurity scattering induced enhancement of T_c has earlier been reported in In-doped SnTe .⁶² Also, SC persisting at lower P with enhanced T_c in layered chalcogenides upon P -cycling has been discussed in terms of structural irreversibility.^{63,64} In the present study, no intrinsic broadening of the XRD Bragg peaks has been observed upon release of pressure, highlighting the absence of noticeable structural disorder. Note that the resistance anomaly of local disorder is regained with almost unchanged characteristic temperature T^* . This indicates that SC emerges in the low temperature disorder-free tetragonal structure in $\text{Ir}_2\text{In}_8\text{S}$. Although the field-

induced resistance change ($\Delta\rho$) is nearly unchanged after P release, a reduced XMR feature is primarily due to the large residual resistivity. Although the MR at 5K and 7T field in the P -released sample is half of the initial MR, the low T resistance upturn with plateau (the XMR feature) is still observed.⁴⁷ A reduced T_m (~ 27 K at 7T field) is in agreement with the increased T -power law coefficient A_1 , as discussed by Sun et al.²⁵

These observations make P -released $\text{Ir}_2\text{In}_8\text{S}$ a unique system, where a large MR persists above SC T_c . As the SC transition width is significantly broad, zero resistance is not reached down to 1.2K, the lowest T of this measurement. The onset T_c , taken as the temperature with 1% resistance drops from the normal state (shown by dashed line), decreases systematically with increasing magnetic field (both in field-scanning and temperature-scanning mode, Figure 5d,e). The T_c - H_{c2} plot [Figure 5f], when fitted with the Ginzburg-Landau (GL) equation $H_{c2} = H_{c2}(0)[(1 - t^2)/(1 + t^2)]$ with $t = T/T_c$, estimates an upper critical field $H_{c2}(0) \sim 0.75$ T, which is an order smaller than the Pauli limit of $1.84T_c \sim 7.5$ T. The estimated GL coherence length ($\xi_{GL} \sim 10$ nm) is much less than the transport mean free path ($l_m \sim 100$ nm), suggesting the phonon mediated SC in the clean limit. In case of orbital-limited behavior, predicted by Werthamer-Helfand-Hohenberg (WHH) theory for the s -wave superconductor,⁶⁵ the estimated upper critical field $H_{c2}^{orb} \approx 0.7T_c \times (\frac{dH_{c2}}{dT})_{T=T_c} = 0.6$ T. The measured upper critical field thus exceeds the orbital-limited value. A quasi-linear $H_{c2} - T_c$ plot can also be seen within our measured T -range. Such quasi-linear SC behavior of Bi_2Se_3 at high pressure has been ascribed to unconventional spin-orbit coupled superconductivity.⁶⁶ However, measurements at further low temperatures are needed for better understanding of the pair-breaking mechanism in the SC state of $\text{Ir}_2\text{In}_8\text{S}$.

We now focus on the results of magneto-resistance and Hall measurements at various high pressures. Figure 6a shows the transverse magneto-resistance plots at 2.5K, at various pressures up to 7.5 GPa and at 5K upon P -release. The MR value decreases rapidly with increasing pressure (see upper inset in Figure 6a). The power-law field dependence ($MR \propto (\mu_a H)^m$, $m = 1.58$ at 0.5 GPa) is found to change gradually at higher P (see lower inset in Figure 6a), showing P -induced change of the Fermi surface anisotropy. In the orthorhombic phase (at 7.5 GPa), m decreases marginally. Upon release, at 0.2 GPa m returns to the initial value.

The field variations of the Hall resistivity at various pressures are shown in Figure 6b. At low pressures, high field Hall resistivity clearly indicate electron dominated transport, but strong non-linearity and positive Hall resistivity at low field (see inset in Figure 6b) indicates significant high mobility hole contributions. To calculate the pressure dependence of the various carrier density and their mobility, we have analyzed the field dependence of the Hall conductivity σ_{xy} using the two band model fit (Figure 6c). In Figure 6(d,e) are plotted the

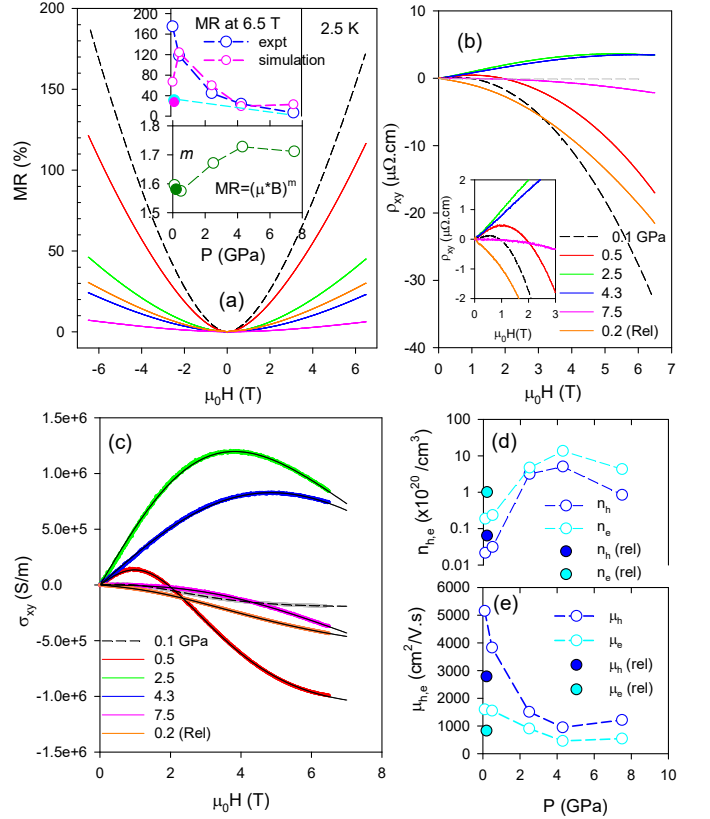


FIG. 6: (Color online) (a) Transverse MR measured at 2.5 K at various quasi-hydrostatic pressures and upon decompression. Upper inset, MR at 6.5 T field plotted as a function of pressure, lower inset, the plot of the exponent for the field variation of the MR as a function of pressure. (b) Hall resistivity plotted as a function of magnetic field at various pressures. (c) Hall conductivity plots $\sigma_{xy}(H)$ and the two-band model fit at various high pressures (d,e) carrier density $n_{e,h}$ and mobility $\mu_{e,h}$ as obtained from the Hall conductivity fit for different pressures. In upper inset in (a), the simulated MR is also plotted based on these carrier density and mobility values. The solid circles in various plots correspond to the decompression data.

pressure variation of the carrier densities ($n_{e,h}$) and mobilities ($\mu_{e,h}$) at 2.5K. With increasing pressures in the tetragonal phase, both carrier densities systematically increase. At low P , the hole density is an order of magnitude less than the electron density, but become roughly of same order above 2 GPa. The hole mobility at low P is a factor of 4 higher than electron mobility, but decreases rapidly at 2 GPa where hole mobility becomes a factor of 1.5 higher than the electron mobility. An enhanced field dependence exponent m (~ 1.72) above 2 GPa can thus be corroborated from the carrier density approaching the same order and also systematic reduction of their mobility mismatch. The carrier densities decrease rapidly in the orthorhombic phase (at 7.5 GPa). Upon releasing P to 0.2 GPa, the carrier densities remain at an order of magnitude high value and the carrier mobility remains

at a relatively low value as compared to the initial P values, indicating the irreversible modification of the Fermi surface pockets in the P -cycled sample.

In the two-band model the magneto-resistance is represented by the equation⁵⁶:

$$MR = \frac{n_e n_h \mu_e \mu_h (\mu_e + \mu_h)^2 B^2}{(\mu_e n_e + \mu_h n_h)^2 + B^2 \mu_e^2 \mu_h^2 (n_e - n_h)^2}$$

We have calculated the MR at 2.5K using the values of carrier density and mobility obtained from the Hall conductivity fit and have compared with the measured values (see upper inset of Figure 6a). Interestingly, the observed MR values at all pressures (including that upon decompression), except at the lowest pressure are in good agreement with the semi-classical two-band model. So the Dirac points have little influence on the mobility at higher P . A significant deviation at low pressure (exhibiting large MR and high hole mobility) may have an origin beyond the classical description. A topological origin or the SOC-coupled orbital texture may have significant role in the enhanced transport mobility at low P which demand further theoretical and experimental investigations. Although the MR (above SC T_c) in the P -released sample shows XMR-like feature, its transport behavior follows the simple two-band model suggesting involvement of trivial bands. However, as the system returns to the initial crystal structure, we cannot rule out the presence of Dirac like band crossings near the Fermi level even in the presence of the enhanced impurity scattering. On the other hand, the observed enhanced carrier density indicates SC onset may be driven by the enhanced DOS at the Fermi level. This may also cause shifting of the Fermi level towards the Dirac point, suggesting possible coexistence of SC and Dirac cones. Our results thus call for direct investigations on the P -released $\text{Ir}_2\text{In}_8\text{S}$ by ARPES measurements. As the zero-resistance has not been observed in SC state in the P -released sample, further investigations at lower T will help understand its SC properties, especially if the SC is of filamentary nature. Signature of unconventional nature of the observed

SC also suggests for point contact spectroscopic investigation to probe for its possible origin in the topological surface states.

IV. CONCLUSIONS

The structural and magneto-transport properties of the type-II Dirac semimetal candidate $\text{Ir}_2\text{In}_8\text{S}$ have been investigated under high pressure. The ambient tetragonal structure with four fold screw symmetry that protects Dirac points is found to be stable up to ~ 7 GPa. In the low pressure phase, a significant change in magneto-transport behavior with increasing T suggests systematic electronic structural modification. Surprisingly, upon release of pressure a sharp resistance drop below ~ 4 K is observed, field dependent studies on which verifies it as the onset of superconductivity. High pressure magneto-transport measurements show irreversible changes of the carrier density and mobility in the pressure-released tetragonal phase, suggesting an irreversible electronic structural modification. The enhanced impurity scattering may have an important role in the emergence of superconductivity in the ambient tetragonal structure (that hosts type-II Dirac semimetal state), making it an ideal platform to study topological superconductivity and Majorana physics. Present results will invite investigations to explore possible emergence of SC in other topological semimetals upon P -cycling by enhancing impurity scattering in an irreversible manner, retaining the structural symmetry and so the topological band structure.

Acknowledgments

High pressure XRD investigations have been performed at Elettra synchrotron, Trieste under the proposal id 20195289. Financial support from DST, Government of India is gratefully acknowledged.

* E-mail: spallavi@barc.gov.in

¹ S. M. Young, S. Zaheer, J. C. Y. Teo, C. L. Kane, E. J. Mele, and A. M. Rappe, Phys. Rev. Lett. **108**, 140405 (2012).

² Q. Wang, Y. Xu, R. Lou, Z. Liu, M. Li, Y. Huang, D. Shen, H. Weng, S. Wang, and H. Lei, Nat. Commun. **9**, 3681 (2018).

³ M. Neupane, S.-Y. Xu, R. Sankar, N. Alidoust, G. Bian, C. Liu, I. Belopolski, T.-R. Chang, H.-T. Jeng, H. Lin, et al., Nat Commun **5**, 3786 (2014).

⁴ T. Liang, Q. Gibson, M. N. Ali, M. Liu, R. J. Cava, and N. P. Ong, Nature Mater **14**, 280 (2015).

⁵ J. Xiong, S. K. Kushwaha, T. Liang, J. W. Krizan, M. Hirschberger, W. Wang, R. J. Cava, and N. P. Ong, Science **350**, 413 (2015).

⁶ J. Xiong, S. Kushwaha, J. Krizan, T. Liang, R. J. Cava, and N. P. Ong, Euro Phys. Lett. **114**, 27002 (2016).

⁷ M. Novak, S. Sasaki, K. Segawa, and Y. Ando, Phys. Rev. B **91**, 041203(R) (2015).

⁸ W. Gao, N. Hao, F.-W. Zheng, W. Ning, M. Wu, X. Zhu, G. Zheng, J. Zhang, J. Lu, H. Zhang, et al., Phys. Rev. Lett. **118**, 256601 (2017).

⁹ S. Y. Xu, C. Liu, S. K. Kushwaha, R. Sankar, J. W. Krizan, I. Belopolski, M. Neupane, G. Bian, N. Alidoust, T. R. Chang, et al., Science **347**, 294 (2015).

¹⁰ X. Huang, L. Zhao, Y. Long, P. Wang, D. Chen, Z. Yang, H. Liang, M. Xue, H. Weng, Z. Fang, et al., Phys. Rev. X **5**, 031023 (2015).

¹¹ C. Shekhar, A. K. Nayak, Y. Sun, M. Schmidt, M. Nicklas, I. Leermakers, U. Zeitler, Y. Skourski, J. Wosnitza, Z. Liu,

- et al., Nat. Phys. **11**, 645 (2015).
- 12 C. Zhang, C. Guo, H. Lu, X. Zhang, Z. Yuan, Z. Lin, J. Wang, and S. Jia, Phys. Rev. B **92**, 041203(R) (2015).
 - 13 N. J. Ghimire, Y. Luo, M. Neupane, D. J. Williams, E. D. Bauer, and F. Ronning, J. Phys.: Condens. Matter **27**, 152201 (2015).
 - 14 M. N. Ali, J. Xiong, S. Flynn, J. Tao, Q. D. Gibson, L. M. Schoop, T. Liang, N. Haldolaarachchige, M. Hirschberger, N. P. Ong, et al., Nature **514**, 205 (2014).
 - 15 L. R. Thoutam, Y. L. Wang, Z. L. Xiao, S. Das, A. Luican-Mayer, R. Divan, G. W. Crabtree, and W. K. Kwok, Phys. Rev. Lett. **115**, 046602 (2015).
 - 16 A. Wang, D. Graf, Y. Liu, Q. Du, J. Zheng, H. Lei, and C. Petrovic, Phys. Rev. B **96**, 121107(R) (2017).
 - 17 R. Schonemann, N. Aryal, Q. Zhou, Y.-C. Chiu, K.-W. Chen, T. J. Martin, G. T. McCandless, J. Y. Chan, E. Manousakis, and L. Balicas, Phys. Rev. B **96**, 121108(R) (2017).
 - 18 F. C. Chen, H. Y. Lv, X. Luo, W. J. Lu, Q. L. Pei, G. T. Lin, Y. Y. Han, X. B. Zhu, W. H. Song, and Y. P. Sun, Phys. Rev. B **94**, 235154 (2016).
 - 19 X. Wang, X. Pan, M. Gao, J. Yu, J. Jiang, J. Zhang, H. Zuo, M. Zhang, Z. Wei, W. Niu, et al., Adv. Electron. Mater. p. 1600228 (2016).
 - 20 M. Ali, L. M. Schoop, C. Garg, J. M. Lippmann, E. Lara, B. Lotsch, and S. S. P. Parkin, Sci. Adv. **2**, e1601742 (2016).
 - 21 R. Singha, A. K. Pariari, B. Satpati, and P. Mandal, Proc. Natl. Acad. Sci. USA **114**, 2468 (2017).
 - 22 E. Mun, H. Ko, G. J. Miller, G. D. Samolyuk, S. L. Budko, and P. C. Canfield, Phys. Rev. B **85**, 035135 (2012).
 - 23 Y. L. Wang, L. R. Thoutam, Z. L. Xiao, J. Hu, S. Das, Z. Q. Mao, J. Wei, R. Divan, A. Luican-Mayer, G. W. Crabtree, et al., Phys. Rev. B **92**, 180402(R) (2015).
 - 24 L.-K. Zeng, R. Lou, D.-S. Wu, Q. N. Xu, P.-J. Guo, L.-Y. Kong, Y.-G. Zhong, J.-Z. Ma, B.-B. Fu, P. Richard, et al., Phys. Rev. Lett. **117**, 127204 (2016).
 - 25 S. Sun, Q. Wang, P.-J. Guo, K. Liu, and H. Lei, New J. Phys. **18**, 082002 (2016).
 - 26 O. Pavlosiuk, P. Swatek, D. Kaczorowski, and P. Wisniewski, Phys. Rev. B **97**, 235132 (2018).
 - 27 Z. Wang, Y. Zheng, Z. Shen, Y. Lu, H. Fang, F. Sheng, Y. Zhou, X. Yang, Y. Li, C. Feng, et al., Phys. Rev. B **93**, 121112(R) (2016).
 - 28 C.-L. Zhang, Z. Yuan, Q.-D. Jiang, B. Tong, C. Zhang, X. C. Xie, and S. Jia, Phys. Rev. B **95**, 085202 (2017).
 - 29 J. Jiang, F. Tang, X. C. Pan, H. M. Liu, X. H. Niu, Y. X. Wang, D. F. Xu, H. F. Yang, B. P. Xie, F. Q. Song, et al., Phys. Rev. Lett. **115**, 166601 (2015).
 - 30 X. H. Niu, D. F. Xu, Y. H. Bai, Q. Song, X. P. Shen, B. P. Xie, Z. Sun, Y. B. Huang, D. C. Peets, and D. L. Feng, Phys. Rev. B **94**, 165163 (2016).
 - 31 F. F. Tafti, Q. Gibson, S. Kushwaha, J. W. Krizan, N. Haldolaarachchige, and R. J. Cava, Proc. Natl. Acad. Sci. USA p. E3475 (2016).
 - 32 H. Huang, S. Zhou, and W. Duan, Phys. Rev. B **94**, 121117(R) (2016).
 - 33 M. Yan, H. Huang, K. Zhang, E. Wang, W. Yao, K. Deng, G. Wan, H. Zhang, M. Arita, H. Yang, et al., Nat. Commun. **8**, 257 (2017).
 - 34 T.-R. Chang, S.-Y. Xu, D. S. Sanchez, W.-F. Tsai, S.-M. Huang, G. Chang, C.-H. Hsu, G. Bian, I. Belopolski, Z.-M. Yu, et al., Phys. Rev. Lett. **119**, 026404 (2017).
 - 35 J. Alicea, Y. Oreg, G. Refael, F. von Oppen, and M. P. A. Fisher, Nat. Phys. **7**, 412 (2011).
 - 36 F. Fei, X. Bo, R. Wang, B. Wu, J. Jiang, D. Fu, M. Gao, H. Zheng, Y. Chen, X. Wang, et al., Phys. Rev. B **96**, 041201(R) (2017).
 - 37 O. J. Clark, M. J. Neat, K. Okawa, L. Bawden, I. Markovic, F. Mazzola, J. Feng, V. Sunko, J. M. Riley, W. Meevasana, et al., Phys. Rev. Lett. **120**, 156401 (2018).
 - 38 F. Fei, X. Bo, P. Wang, J. Ying, J. Li, K. Chen, Q. Dai, B. Chen, Z. Sun, M. Zhang, et al., Adv. Mater. p. 1801556 (2018).
 - 39 L. He, Y. Jia, S. Zhang, X. Hong, C. Jin, and S. Li, npj Quantum Materials **1**, 16014 (2016).
 - 40 D. Kang, Y. Zhou, W. Yi, C. Yang, J. Guo, Y. Shi, S. Zhang, Z. Wang, C. Zhang, S. Jiang, et al., Nat. Commun. **6**, 7804 (2015).
 - 41 X.-C. Pan, X. Chen, H. Liu, Y. Feng, Z. Wei, Y. Zhou, Z. Chi, L. Pi, F. Yen, F. Song, et al., Nat. Commun. **6**, 7805 (2015).
 - 42 E. Liu, Y. Sun, N. Kumar, L. Muechler, A. Sun, L. Jiao, S.-Y. Yang, D. Liu, A. Liang, Q. Xu, et al., Nat. Phys. **14**, 1125 (2018).
 - 43 J. F. Khoury, A. J. E. Rettie, M. A. Khan, N. J. Ghimire, I. Robredo, J. E. Pfluger, K. Pal, C. Wolverton, A. Bergara, J. S. Jiang, et al., J. Am. Chem. Soc. **141**, 19130 (2019).
 - 44 J. F. Khoury, A. J. E. Rettie, I. Robredo, M. J. Krogstad, C. D. Malliakas, A. Bergara, M. G. Vergniory, R. Osborn, S. Rosenkranz, D. Y. Chung, et al., J. Am. Chem. Soc. **142**, 6312 (2020).
 - 45 T. Sakamoto, M. Wakeshima, Y. Hinatsu, and K. Matsuhira, Phys. Rev. B **75**, 060503(R) (2007).
 - 46 T. Sakamoto, M. Wakeshima, Y. Hinatsu, and K. Matsuhira, Phys. Rev. B **78**, 024509 (2008).
 - 47 See supplemental material [http://] for synthesis, chemical composition analysis, structural characterization by XRD, HRTEM, additional plots and data of high pressure XRD analysis and resistance and magneto-resistance plots upon decompression.
 - 48 A. Dewaele, P. Loubeyre, and M. Mezouar, Phys. Rev. B **70**, 094112 (2004).
 - 49 A. Hammersley, *Computer Program FIT2D* (ESRF, Grenoble, 1998).
 - 50 A. C. Larson and R. B. von Dreele, *Report No. LAUR 86-748* (Los Alamos National Lab, New Mexico, 1986).
 - 51 M. Ziman, *Electrons and Phonons* (Clarendon Press, Oxford, 1962).
 - 52 H. Takatsu, J. J. Ishikawa, S. Yonezawa, H. Yoshino, T. Shishidou, T. Oguchi, K. Murata, and Y. Maeno, Phys. Rev. Lett. **111**, 056601 (2013).
 - 53 K. Wang, D. Graf, L. Li, L. Wang, and C. Petrovic, Sci. Rep. **4**, 7328 (2014).
 - 54 Resistivity upturn appears in XMR materials below $T_m = \hbar c B / m^* k_B$, where m^* is the average effective mass. In $\text{Ir}_2\text{In}_8\text{S}$, $m^* \sim 0.3 m_e$ and so $T_m \sim 50\text{K}$ at 7 T field.
 - 55 P. L. Cai, J. Hu, L. P. He, J. Pan, X. C. Hong, Z. Zhang, J. Zhang, J. Wei, Z. Q. Mao, and S. Y. Li, Phys. Rev. Lett. **115**, 057202 (2015).
 - 56 A. B. Pippard, *Magnetoresistance in Metals* (Cambridge University Press, Cambridge, UK, 1989).
 - 57 O. Pavlosiuk and D. Kaczorowski, Sci. Rep. **8**, 11297 (2018).
 - 58 X. Li, J. Sun, P. Shahi, M. Gao, A. H. MacDonald, Y. Uwatoko, T. Xiang, J. B. Goodenough, J. Cheng, and J. Zhou, Proc. Natl. Acad. Sci. USA **115**, 9935 (2018).

- ⁵⁹ N. Kumar, C. Shekhar, S.-C. Wu, I. Leermakers, O. Young, U. Zeitler, B. Yan, and C. Felser, Phys. Rev. B **93**, 241106(R) (2016).
- ⁶⁰ F. Han, J. Xu, A. S. Botana, Z. L. Xiao, Y. L. Wang, W. G. Yang, D. Y. Chung, M. G. Kanatzidis, M. R. Norman, G. W. Crabtree, et al., Phys. Rev. B **96**, 125112 (2017).
- ⁶¹ C. M. Hurd, *The Hall Effect in Metals and Alloys* (Cambridge University Press, Cambridge, UK, 1972).
- ⁶² M. Novak, S. Sasaki, M. Kriener, K. Segawa, and Y. Ando, Phys. Rev. B **88**, 140502(R) (2013).
- ⁶³ F. Ke, H. Dong, Y. Chen, J. Zhang, C. Liu, J. Zhang, Y. Gan, Y. Han, Z. Chen, C. Gao, et al., Adv. Mater. **29**, 1701983 (2017).
- ⁶⁴ U. Dutta, P. S. Malavi, S. Sahoo, B. Joseph, and S. Kar-makar, Phys. Rev. B **97**, 060503(R) (2018).
- ⁶⁵ N. R. Werthamer, E. Helfand, and P. C. Hohenberg, Phys. Rev. **147**, 295 (1966).
- ⁶⁶ K. Kirshenbaum, P. S. Syers, A. P. Hope, N. P. Butch, J. R. Jeffries, S. T. Weir, J. J. Hamlin, M. B. Maple, Y. K. Vohra, and J. Paglione, Phys. Rev. Lett. **111**, 087001 (2013).